# DEVELOPMENT AND CHARACTERIZATION OF NMR AND MRI METHODS FOR ASSESSMENT OF TUMOR OXYGEN CONSUMPTION

By

Joshua Banks

Thesis

Submitted to the Faculty of the

Graduate School of Vanderbilt University

in partial fulfillment of the requirements

for the degree of

MASTER OF SCIENCE

in

Physics

December, 2012

Nashville, Tennessee

Approved

Professor C. Chad Quarles

Professor Daniel F. Gochberg

## TABLE OF CONTENTS

## LIST OF FIGURES

## LIST OF TABLES

Table Page

# CHAPTER 1

# INTRODUCTION

## 1.1 Research Motivation

Seventy years ago, Otto Warburg observed that cancer cells metabolize glucose in a way that is very distinct from normal cells. He demonstrated that even that in the presence of oxygen, highly metabolic cancer cells primarily generate adenosine -5' triphosphate (ATP), the energy currency of cells, via glycolysis (1). Given the high metabolism of tumor cells, this phenomenon is counterintuitive because glycolysis is an extremely inefficient way to generate high quantities of (ATP) and ultimately results in increased lactate production and acidification of the tumor microenvironment. Since this discovery, the characterization of tumor metabolic features remains a very active area of research.

At a basic level cellular energetics involves both oxidative and non-oxidative pathways. The main non-oxidative pathways are glycolysis and lactic acid fermentation and the major oxidative pathways are the tricarboxcylic acid (TCA) cycle and oxidative phosphorylation. In the presence of oxygen, normal cells tend to go through glycolysis, the TCA cycle and oxidative phosphorylation, respectively (**Figure 1**). During the TCA cycle, glucose is converted into pyruvate in the cytoplasm of the cells. Pyruvate is then decarboxylated to form acyetyl-CoA, which is further metabolized in the mitochondria of cells, via the TCA cycle. During the TCA cycle, cells take in oxygen to produce carbon dioxide, water, and ATP in addition to a number of other intermediates along the way. The most important of these intermediates include NADH and $FADH_2$, which donate electrons to molecular oxygen in a process termed the electron transport

chain. The free energy released by the removal of these electrons is used to transport protons from the mitochondrial matrix to the external cystol. This, in turn, forms a proton gradient between the cystol and mitochondrial matrix, which is used by the protein ATP synthase, to create ATP. The last step of the electron transport chain combined with the synthesis of ATP is termed oxidative phosphorylation. The net reaction for the oxidative pathways (TCA cycle and oxidative phosphorylation combined) is:

$$H_3CCOO^- + 2O_2 + H^+ \rightarrow \text{metabolites} \rightarrow 2CO_2 + 2H_2O + 36ATP \quad (1)$$

In the absence of oxygen, cells tend to bypass the TCA cycle and oxidative phosphorylation and instead produce ATP energy primarily through glycolysis. In contrast to normal tissue, cancer cells tend to use glycolysis for ATP production even in the presence of oxygen. In fact, cancer cells produce 85% of their energy from glycolysis and only 15% from oxidative pathways (**Figure 2**). Unlike aerobic respiration, which produces 36 ATP per glucose, glycolysis only results in the formation of 4 total (2 net) molecules of ATP (1). Thus, to generated ATP, tumor cells consume large amounts of glucose (1).

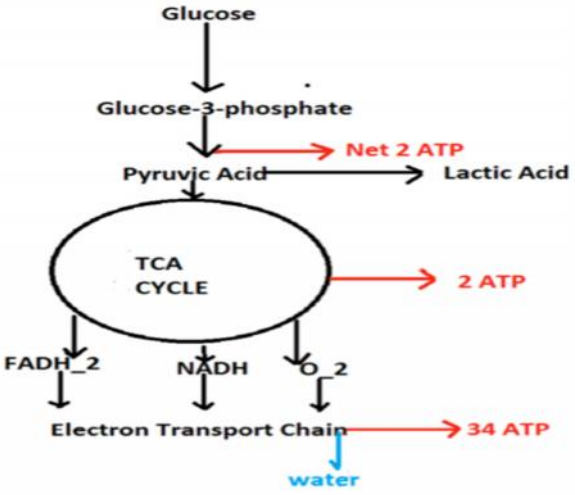


**Figure 1**: Cellular metabolism of glucose via glycolysis and oxidative phosphorylation. During glycolysis, glucose is metabolized to pyruvate. Under aerobic conditions the pyruvate goes through the Tricarboxcylicacid(Krebs) cycle.Source:http://webanatomy.net/anatomy/aerobic.jpg

Several studies have shown that there is a clear connection between the aggressiveness and metastatic potential of cancer and increased glycolysis (or abnormal oxidative metabolism) (2).

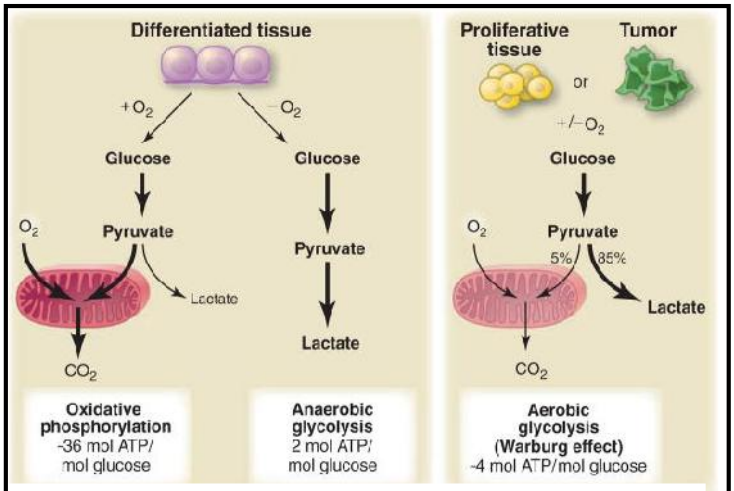


**Figure 2**: Diagram showing the metabolic differences between normal tissue and tumors(1).

Thus, the development of techniques to assess metabolism and oxygen use within cancer is highly relevant. Such methods could enable improved characterization of tumor metabolic properties and new clinical tools to evaluate disease status and monitor treatment response.

Across the range of imaging modalities methods exist to assess local oxygen tension and/or oxygen metabolism. Optical techniques can be used to measure tissue oxygenation through the conjugation of fluorescent agents to compounds that are sensitive to cellular oxygen tension. For example, nitroimidazole derivatives are the most commonly used agents for the immunohistochemical evaluation of hypoxia in *ex vivo* tissue samples or *in vitro* cell cultures. Such agents are selectively reduced and retained within hypoxia tissue (3). The attachment of a fluorescent agent to such compounds enables their localization and quantification within tissue. Florescent methods can also be used to measure the fluorescence lifetime of many optical probes are proportional to the concentration of dissolved oxygen in tissue and can thereby be used to assess the partial pressure of oxygen ($pO_2$) (3).

Positron Emission Tomography (PET) can also be used to assess tissue oxygenation and oxygen utilization *in vivo*. Similar to the fluorescent agents described above, PET agents which are created from imidazole derivatives can be used to detect local tissue hypoxia (4). The rate of oxygen utilization within tissue can also be assessed through the use of $^{15}O_2$ gas. When inhaled, $^{15}O_2$ can serve as an indicator of oxidative phosphorylation by measuring the rate at which $^{15}O_2$ is metabolized to $H_2{}^{15}O$. However, since PET is sensitive to $^{15}O_2$ in all its chemical forms, it is unable to distinguish between the $^{15}O_2$ bound to hemoglobin and $^{15}O_2$ covalently attached to the water produced by oxidative phosporylation (5). This presents a fundamental limitation of using PET to assess tumor oxygen utilization.

Similar to $^{15}O_2$ for PET, $^{17}O_2$ can be used as to assess oxygen utilization for NMR (Nuclear Magnetic Resonance) and MRI (Magnetic Resonance Imaging) applications. This is because the rate at which $^{17}O_2$ is metabolized to $H_2{}^{17}O$, can be measured by these magnetic resonance techniques. Unlike PET, $^{17}O$ MRI and NMR only detect the $^{17}O$ covalently bound to water. Whereas other methods primarily evaluate oxygen tension, $^{17}O$ methods are unique from a biochemical perspective because they have the potential to directly access oxidative phosphorylation by measuring the rate that "metabolic" water is being produced.

The primary use of $^{17}O$ MRI methods has been in the field of neuroscience. The focus of these studies has been the measurement of the $CMRO_2$ (Cerebral Metabolic Rate of Oxygen Consumption) via quantification of $H_2{}^{17}O$ production. In many neurological conditions, such as Alzheimer's and Parkinson's disease, cytochrome c oxidase, the enzyme that catalyzes the reduction of oxygen to water, is impaired (5). Thus, the assessment of the $CMRO_2$, could shed new insights into the pathology of these diseases and be a useful clinical indicator of diseases status.

As described above, oxidative phosphorylation is implicated in malignant tumors. Thus, measuring a tumor's oxygen consumption could also yield information that is useful from both a clinical and basic science standpoint. The long-term goal of our research is to develop $^{17}O$ methods to study the abnormal oxygen consumption within tumors. An important step towards this goal is the validation of methods that are capable of quantifying changes in $H_2{}^{17}O$ content within tissue. Currently, the most commonly used approach to quantify $H_2{}^{17}O$ content *in vivo* is through the use of $T_{1\rho}$ –weighted imaging sequences. As described below, the reliability of this approach, in the context of cancer, may be confounded by variations in tissue pH, $T_1$ and $T_2$. **Thus, the goals of this study were to characterize the influence of tissue acidity and heterogeneous $T_1$ and $T_2$ profiles on $T_{1\rho}$-based measures of $H_2{}^{17}O$ concentration.** To achieve this goal we investigated protein phantoms with varying degrees of $H_2{}^{17}O$, Gd-DTPA (Gadopentetic acid), and pH levels. To provide the basis for $T_{1\rho}$ imaging methods of $^{17}O$ water we briefly review the theoretical basis of NMR.

### 1.2 Theoretical Basis of NMR/MRI

NMR spectroscopy and MRI imaging can be understood in terms of classical mechanics. In the classical picture of NMR, the atoms that constitute a chemical substance can be collectively viewed as an NMR ensemble. Each of the atoms in the ensemble has an individual magnetic moment. When placed in an external magnetic field, such as that used during a MRI or NMR experiment, the ensemble of magnetic moments will precess about the applied field. The frequency of the precession is given by the Lamor equation, $\omega_0=\gamma B_0$ where $\gamma$ is the gyromagnetic ratio and $B_0$ is the static magnetic field strength.

The individual magnetic moments can be resolved into x, y, and z components. For our purposes, we will define the direction of the applied magnetic field ($B_0$) as oriented along the z-axis. The z –components can either be oriented such that it is aligned with the positive or negative z-axis. In an NMR ensemble, more molecules have z components in the positive direction than the negative direction. As a result, the net magnetic moment or magnetization is aligned with the positive z-axis is at thermal equilibrium. The x and y components of the individual magnetic moments can have a range of values and phases and can have positive or negative orientations along their respective axes. For an NMR ensemble in thermal equilibrium, each atom is equally likely to have a x or y component in the positive direction as in the negative direction. As a result, there are is an equal probability of the magnetization aligning in the positive direction as in the negative direction in transverse plane. Consequently, the net magnetic moment cancels out in both the x and y directions.

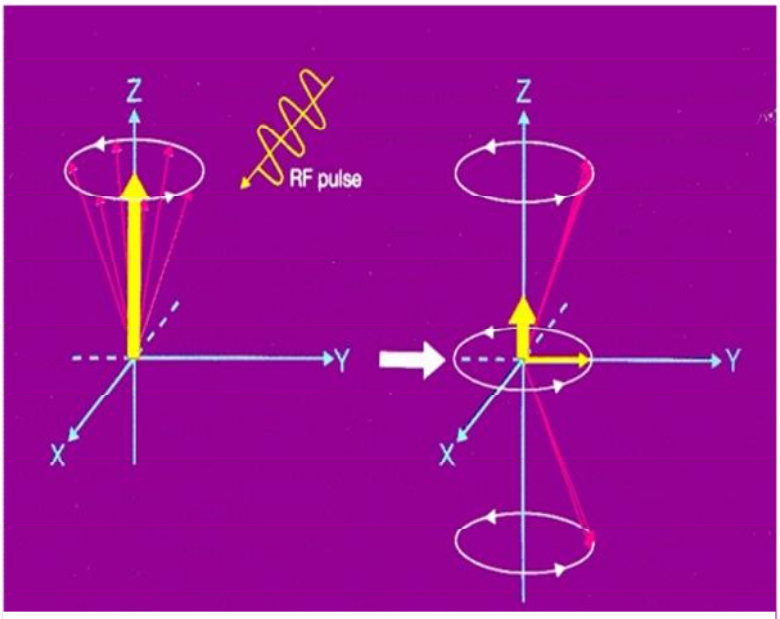


**Figure 3**: a) The net magnetization points in the z-direction. b) A RF pulse is applied flips the magnetization into the x-y plane. Source http://web.mit.edu/hst.583/

The resonance phenomenon occurs when a radiofrequency (RF) pulse is applied perpendicular to the static field (see **Figure 3**). This results in a torque that tips the magnetization into the transverse plane. The angle of the magnetization with respect to the z-axis increases with the

duration of the RF pulse. The magnetic resonance phenomenon occurs when the angular frequency of the RF pulse equals the Larmor frequency.

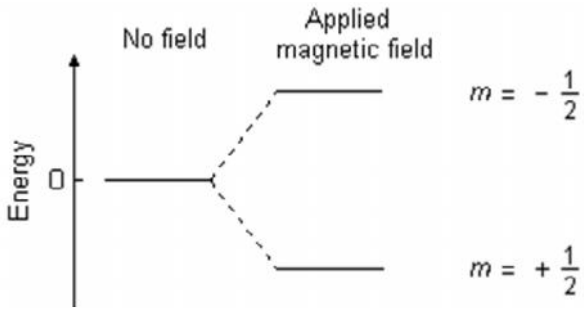


**Figure 4:** When a static magnetic field is applied along the z-axis the single energy level of a spin ½ particle splits into two. Magnetic resonance occurs when the frequency of a perturbing field equals the energy difference between the two levels.

The quantum mechanical analog to the two z orientations of the magnetic moment is that there are two spin states which correspond to two different energies in a static field. These spin states are $m_z$=+1/2, which corresponds to the highest energy state, and $m_z$=-1/2, which corresponds to the lowest state (**Figure 4**). Because the oscillating magnetic field due to the RF pulse is small and time varying, it corresponds to a perturbation in the quantum mechanical sense. According to Fermi's Golden Rule in quantum mechanics, the presence of the perturbation introduces a transition probability between the lower and upper states. This transition between energy levels when the resonance condition is fulfilled corresponds to the rotation of the net magnetic moment caused by the torque in the classical picture. The probability that a spin in an ensemble of atoms undergoes a transition is given by Rabi's formula as a function of time:

$$P(\tau) = \frac{\omega_1^2}{\omega_1^2+(\Delta\omega)^2} sin^2 \left(\omega_1^2 + (\Delta\omega)^2 \frac{\tau}{2}\right)^{1/2} \quad (2)$$

where $\omega_1$ is the frequency of the RF field, $\Delta\omega$ is the difference between the Larmor frequency and the frequency of the RF field, and $\tau$ is the duration of the pulse. When $\Delta\omega$ equals zero, the resonance condition is fulfilled and a transition occurs between the ground and excited states of a hydrogen nuclei (m=-1/2 and m=+1/2, respectively) **Figure 4**.

Several intrinsic properties of a material that are given by NMR spectroscopy include thelongitudinal relaxation $T_1$, transverse relaxation $T_2$, and $T_{1\rho}$. $T_1$ and $T_2$ are measured in the laboratory frame, which is defined as a coordinate system stationary with respect to the RF pulse. $T_{1\rho}$ on the other hand is measured in the rotating frame, which is defined as the coordinate system rotating at the carrier frequency of the RF pulse. These time constants describe the behavior of the magnetization after it is rotated away from the z-axis by an RF pulse. $T_1$ is the time for the longitudinal magnetization (z-component of magnetization) to recover to 63% of the thermal equilibrium value. The physical mechanism for $T_1$ relaxation is the transfer of energy from excited nuclei in the NMR ensemble to the rotational and translational energies of the surrounding lattice (7). $T_2$ is the time for the transverse magnetization (vector sum of the x-component and y-component of the magnetization) to decay to 37% of its initial value after excitation. Physically, this represents the time for the individual magnetic moments in x y plane to accrue different phases due to different processional frequencies such that they cancel out. Processes that result in these inhomogeneities in the processional frequencies include variation in local magnetic fields in the sample, dipolar coupling, and the orientation dependence of the chemical shift. These physical process that influence $T_2$ also influence another decay constant $T_2^*$. However, $T_2^*$ additionally accounts for the decay due to inhomogeneties in the main magnetic field and the subseptibiltity of the sample. As a result, $T_2^*$ decay of the signal is usually faster than $T_2$ decay. $T_2$ can be recovered by using a spin echo sequence by refocusing these interactions using a spin echo sequence. $T_{1\rho}$ is the time for the bulk magnetization to decay to 37% of its initial value. This decay occurs when there is an application of a spin lock pulse in addition to a 90 degree pulse. Like $T_1$, this effect occurs because of the transfer of energy from

the nuclear spins to the translational and rotational energies of the surrounding atoms. However, unlike $T_1$, this effect is measured in the rotating frame as opposed to the lab frame.

Collectively $T_1$, $T_2$, and $T_{1\rho}$ govern the decay and recovery of the NMR signal during and after the application of a RF pulse. The exponential growth and recovery of the signal can be related to these relaxation parameters by the following equation

$$S = S_0 \left|1 - \exp\left(-\frac{TR}{T_1}\right)\right| \exp\left(-\frac{TE}{T_2}\right) \exp\left(-\frac{TSL}{T_{1\rho}}\right) \quad (3)$$

where TR is the interval at which the pulse sequence is repeated, TE is the time at which a spin echo refocuses the magnetization, and TSL is the time period during which a spin lock pulse is applied. By choosing appropriate values of TR, TE, and TSL, one can make any two out of three of these exponential terms approximately equal to one. This allows the signal to essentially decay according to the argument inside of the surviving exponential. In other words, the signal can be made to be $T_1$, $T_2$, or $T_{1\rho}$–weighted.

Besides relaxation, another intrinsic property of material that can be evaluated by NMR/MRI is chemical shift. Chemical shift is a term used to describe the variations in the resonant frequency experienced by a molecule due to local perturbations created by its electrons circulating though the main magnetic field. Because each molecule has a unique chemical shift, this property is extremely useful in identifying a chemical because it gives each molecule a unique molecular fingerprint. The chemical shift and relaxation properties of $^{17}O$ have important consequences for the in vivo detection of $H_2{}^{17}O$.

The gyromagnetic ratio and the natural abundance of $^{17}O$ have importance implications for magnetic resonance applications. $^{17}O$ has a natural abundance of 0.037% which is 30 times lower

than that of $^{13}C$ and 2700 times lower than the natural abundance of $^{1}H$ (6), making detection and quantification a challenge. The gyromagnetic ratio of $^{17}O$ is about 7.4 times lower than that of $^{1}H$. Because signal strength is proportional to the gyromagnetic ratio, the relatively low gyromagentic ratio of $^{17}O$ creates an additional barrier for detection.

As described above, MR-based detection of $^{17}O$ detection is useful because it can discriminate between metabolically produced $H_2{}^{17}O$ and gaseous $^{17}O_2$. The$^{17}O_2$ bound to hemoglobin has an extremely short $T_2$ due to the slow molecular motion of hemoglobin. Since linewidth and $T_2$ are inversely related, this short transverse relaxation results in an extremely broad linewidth, thus rendering $^{17}O_2$ bound to hemoglobin undetectable through NMR spectroscopy (6). Additionally, the $^{17}O$ gas dissolved in water is undetectable because of the short transverse relaxation because of the dipolar coupling between the unpaired electrons and the nucleus (6).This is particularly useful for studies assessing oxidative phosphorylation because only the $^{17}O$ bound to the $H_2{}^{17}O$ (which is produced through this pathway) will be detectable.

The methods to detect $H_2{}^{17}O$ are generally classified as either direct or indirect (5). The direct detection of $H_2{}^{17}O$ involves the acquisition of signal at its respective chemical shift. The low inherent sensitivity of direct detection (due to the low natural abundance and gyromagentic ratio of $^{17}O$) has posed a fundamental challenge to the development of these techniques. Further, direct detection techniques have limited clinical utility, as it requires the construction of specialized RF detection coils not widely available. Consequently, this has spurred the exploration of indirect methods.

Instead of directly detecting $^{17}O$ resonance at its respective chemical shift, $H_2{}^{17}O$ can also be indirectly detected because of the influence of $H_2{}^{17}O$ on the relaxation of water protons ($^{1}H$).

Unlike the oxygen in $^{16}O$ water, the oxygen in $^{17}O$ water has a non-zero spin magnetic moment and can interact with the $^{1}H$ covalently bound to the water via through bond scalar coupling interactions with $^{17}O$. The scalar coupling is modulated though exchange between the $H_2{}^{17}O$ and $H_2{}^{16}O$ and the magnitude of the modulation is proportional to the amount of $H_2{}^{17}O$ that is present. Thus, indirect methods are sensitive to the local $H_2{}^{17}O$ concentration and can potentially be used for quantification.

The proton imaging of oxygen (PRIMO) method was proposed as a means to indirectly detect $H_2{}^{17}O$ through its effects on the $T_2$ of water protons. This method assumes that the change in $T_2$ of water protons after $H_2{}^{17}O$ or $^{17}O$ administration is related to the amount of $H_2{}^{17}O$ that is delivered or metabolically created within tissue (8). The PRIMO method involves the acquisition of an MR signal which includes the effects of $H_2{}^{17}O$ coupling and one where the effects of scalar coupling are removed by irradiating at the frequency of $^{17}O$. The ratio of the difference between the uncoupled and coupled signals to the uncoupled signal provides an estimate of the amount of $H_2{}^{17}O$ water.

The sensitivity to the exchange of $H_2{}^{17}O$ with $H_2{}^{16}O$ by indirect $T_2$ is obscured by the presence of dipole interactions and diffusion (9). As a consequence, although PRIMO has relatively high sensitivity, there are still challenges for the in vivo $H_2{}^{17}O$ quantification using this method. An alternative approach to indirectly detect $H_2{}^{17}O$ is through the use of a $T_{1\rho}$-weighted sequence (9). The application of a spin pulse in this sequence attenuates process other than exchange. Exchange, rather than other biophysical mechanisms such as diffusion and dipolar coupling, is the primary modulator of $T_{1\rho}$. Consequently, the isolation of exchange in a $T_{1\rho}$ weighted sequence allows for an increase in the dynamic range of $T_{1\rho}$ relative to $T_2$(9).

In a $T_{1\rho}$ -weighted sequence, the signal no longer decays according to $T_2$ as in the PRIMO method, but according to the local $T_{1\rho}$. The amplitude of the spin locking pulse can be varied to yield different $T_{1\rho}$ relaxation rates. The spin lock pulse causes the individual magnetic moments to process around $B_1$according to $\omega_1=\gamma B_1$. Thus, $B_1$ plays the role of $B_0$ in the case of a spin lock pulse. As a consequence, the spin lock pulse can be expressed in units of frequency or amplitude. A plot of $T_{1\rho}$ versus spin lock amplitude is typically termed a $T_{1\rho}$ dispersion curve.

The $T_{1\rho}$ dispersion approaches $T_2$ as the spin lock frequency approaches 0 and $T_1$ as the spin lock frequency approaches the Larmor frequency. As a result, $T_{1\rho}$ is influenced by processes that affect $T_1$ and $T_2$ (10). In particular, the difference in chemical shift between the two sites a sample between which the proton is changing modulates both of these decay constants. This is because in the equation governing two-site exchange for both $T_{1\rho}$ and $T_2$, the frequency offset between the two exchanging species appears(7). $T_{1\rho}$ is typically longer than $T_2$ because the spin locking pulse reduces the affects of dephasing on the MR signal. From the perspective of molecular dynamics the $T_{1\rho}$ bears some semblance to $T_1$, because, it involves the transfer of energy from the ensemble to the lattice as with $T_1$. However, this exchange occurs at the spin lock frequency in the case of $T_{1\rho}$ and at the Larmor frequency in the case of $T_1$. The relative number of lattice modes available for exchange is much greater at clinically relevant spin lock frequencies, which are typically much lower than the Larmor frequency(10).

### 1.3 T1ρ spectroscopy

Previous studies have shown that $H_2{}^{17}O$ concentration can be determined by acquiring $T_{1\rho}$ values at two spin lock frequencies. Similar to the PRIMO method, the two frequency $T_{1\rho}$ approach relies up acquiring data with and without the effects of exchange between $H_2{}^{17}O$ and $H_2{}^{16}O$. The

low spin lock frequency exhibits a high sensitivity to exchange, whereas the high frequency pulse diminishes the effect of proton exchange (11, 12). Thus, the relaxivity of $H_2{}^{17}O$ increases with decreasing spin lock frequency.

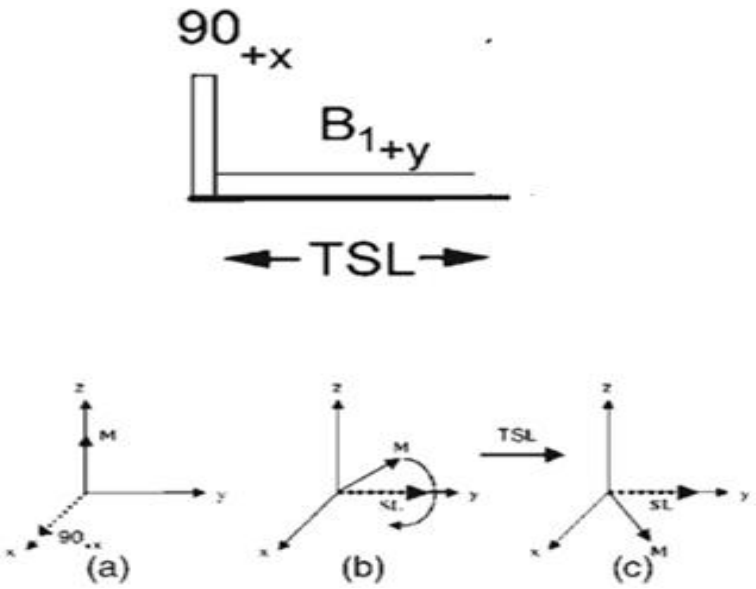


**Figure 5:** When a static magnetic field is applied along the z-axis the single energy level of a spin ½ particle splits into two. Magnetic resonance occurs when the frequency of a perturbing field equals the energy difference between the two levels.

To extract these values, the MR signal has to be acquired at multiple spin locking times (TSL) for each frequency. These signal decays can be fit to the following expression:

$$S = S_0 exp(-\frac{TSL}{T_{1\rho}}) \quad (4)$$

in order to extract the $T_{1\rho}$ values. **Figure 5** shows a typical pulse sequence used to acquire such data. This procedure can then be repeated for several frequencies in order to create a $T_{1\rho}$ vs. frequency dispersion curve.

The effect of $H_2{}^{17}O$ on$T_{1\rho}$ is given by the following equation (13):

$$\frac{1}{T_{1\rho(\omega 1)}} = \frac{1}{T^0_{1\rho}} + \frac{(\frac{35}{12})\tau J^2 C}{1+\tau^2\omega_1^2} \quad (5)$$

Where $T^0_{1\rho}$ is the relaxation rate of the water protons independent of $H_2{}^{17}O$, $\tau$ is the proton exchange time characterizing the exchange between the two isotopes of water and $C$ is the $H_2{}^{17}O$

concentration in the sample, and $\omega_1$ is the processional frequency (or equivalently the amplitude of the RF pulse) in the rotating frame. *J* is the coupling constant between $^1H$ and $^{17}O$ in water.

Recall that $H_2{}^{17}O$ content can be determined using a low and high spin locking power. By combining Eqs (4) and (7) the ratio of concentrations of $H_2{}^{17}O$ between an enriched and unenriched phantom, $f_E/f_{NA}$ can be determined using the following equation(11)

$$\frac{f_E}{f_{NA}} = \frac{Ln(\frac{s_h^t}{s_l^t}) - (TSL)(\frac{1}{T_{1\rho 0}^l} - \frac{1}{T_{1\rho 0}^h})}{Ln(\frac{s_h^{na}}{s_l^{na}}) - (TSL)(\frac{1}{T_{1\rho 0}^l} - \frac{1}{T_{1\rho 0}^h})} \quad (6)$$

where $s_h^t$ is the signal at a high spin lock power, $s_l^t$is the signal at a low spin lock power, $S_h^{na}$ is the baseline natural abundance signal atthe high spin lock power and $s_l^{na}$is the baseline natural - abundance signal at the low spin lock power. TSL is the time period during which the magnetization is locked by the RF pulse. $T_{1\rho 0}^l$ and $T_{1\rho 0}^h$ are the intrinsic relaxation rates independent of $H_2{}^{17}O$ concentration acquired at low and high spin locking frequencies, respectively.

In the context of an *in vivo* study, this approach can be used to track the time dependent change in the concentration of $H_2{}^{17}O$ due to inhalation and metabolism of $^{17}O_2$. This equation can also be applied to *in vitro* studies where the time dependent change in $H_2{}^{17}O$ can be mimicked by the use of phantoms enriched with $H_2{}^{17}O$ water. In addition to the quantitative information that can be obtained from the changes in the MRI signal due to $H_2{}^{17}O$ enrichment, one can also observe changes the amount of dispersion (difference between the $T_{1\rho}$ values of the upper and lower extrema of a dispersion curve). This is because an increase in the concentration of $H_2{}^{17}O$

increases the amount of exchange between $H_2{}^{17}O$ and $H_2{}^{16}O$, which in turn modulates the $T_{1\rho}$ values.

The two frequency $T_{1\rho}$ approach has been used to calculate the $H_2{}^{17}O$ concentration in several physiological contexts. Reddy et al quantified the amount of $H_2{}^{17}O$ production due to cerebral oxygen metabolism (12). McCommis et al used the signal decays for a $T_{1\rho}$ weighted pulse sequence to examine the dynamics of $H_2{}^{17}O$ production in myocardial tissue in heart (14). To our knowledge no study has used this approach to evaluate tumor oxygen metabolism.

# CHAPTER 2

## $T_{1\rho}$ STUDIES OF PROTEIN PHANTOMS ENRICHED WITH $H_2{}^{17}O$ WATER

### 2.1 Introduction

As mentioned above, cancer cells often have acidic pH and heterogonous protein profiles. Changes in pH could potentially affect chemical exchange, which, in turn, could impact $T_{1\rho}$ dispersion. Similarly, heterogeneous protein profiles could result in a wide range of $T_1$ and $T_2$ values within a tumor, thereby creating a range of $T_{1\rho}$ dispersion curves. Since the two-frequency $T_{1\rho}$ approach for $H_2{}^{17}O$ quantification has yet to be validated in tumors we sought to address whether these potential changes in $T_{1\rho}$ dispersion could alter its reliability. **Thus, the goals of this study were to characterize the influence of tissue acidity and heterogeneous $T_1$ and $T_2$ profiles on $T_{1\rho}$-based measures of $H_2{}^{17}O$ concentration.**

For our studies we created a series of Bovine Serum Albumin (BSA) phantoms with variable $H_2{}^{17}O$ concentration, pH, $T_1$ and $T_2$. The eight phantoms we used are listed in Table 1.

**Table 1**: Protein phantoms used in our studies. Note 0.037% is natural abundance of $H_2{}^{17}O$ and 0.1480% is four time the natural abundance.

| Phantom # | BSA Content | GdDTPA concentration | pH level | $H_2{}^{17}O$ content |
|---|---|---|---|---|
| 1) | 7% | 0mM | 7.4 | 0.037% |
| 2) | 7% | 0mM | 7.4 | 0.1480% |
| 3) | 7% | 0mM | 5.6 | 0.037% |
| 4) | 7% | 0mM | 5.6 | 0.1480% |
| 5) | 7% | 0.25mM | 7.4 | 0.037% |
| 6) | 7% | 0.25mM | 7.4 | 0.1480% |
| 7) | 7% | 0.25mM | 5.6 | 0.037% |
| 8) | 7% | 0.25mM | 5.6 | 0.1480% |

## 2.2 Methods

The $T_{1\rho}$ data was acquired using a Bruker NMR spectrometer operating at 400 MHz. Standard NMR protocols were used for shimming and power calibration. The $T_{1\rho}$ data was acquired using 11 spin lock powers ranging from 128Hz to 10,500Hz. At each spin lock power, the proton spectra of the water molecules was collected for 8 spin locking times from 2.5ms to 1000ms. The NMR signal for each spin locking time was calculated by taking the integrated area of the spectra. The $T_{1\rho}$ values and dispersion curves for each phantom were computed using algorithms written in MATLAB for least squares fitting.

## 2.3 Results

Given the challenges inherent with $H_2{}^{17}O$ detection, we also evaluated the measurement reproducibility across six identical BSA phantoms with a pH 7.4 and natural abundance [$H_2{}^{17}O$]. To assess the agreement across samples we evaluated the Interclass Correlation Coefficient, which describes how closely the $T_{1\rho}$ values resemble each other across each of the six phantoms. The ICC was found to 0.908 or 91% for these phantoms, indicating that these experiments are highly reproducible and deviations from the $T_{1\rho}$ values of these phantoms likely reflect changes in [$H_2{}^{17}O$], pH, $T_1$ and/or $T_2$.

**Figure 6** shows a comparison of $R_{1\rho}$ dispersion curves (where $R_{1\rho} = 1/T_{1\rho}$) in BSA phantoms (pH = 7.4) with $H_2{}^{17}O$ at natural abundance and four times natural abundance (phantoms 1 and 2, respectively, in (**Table 1**). The dispersion curve for phantom 2 was clearly shifted upward due to the enrichment of $H_2{}^{17}O$ (**Figure 6**). The difference between $R_{1\rho}$ values between the two phantoms is much greater at low frequencies than at high frequencies (e.g. 4 times greater at 128Hz than at 10500Hz) consistent with previous results (13). This is because the relative number (spectral density) of protons exchanging at the spin lock frequency is much greater at low frequencies than at high frequencies.

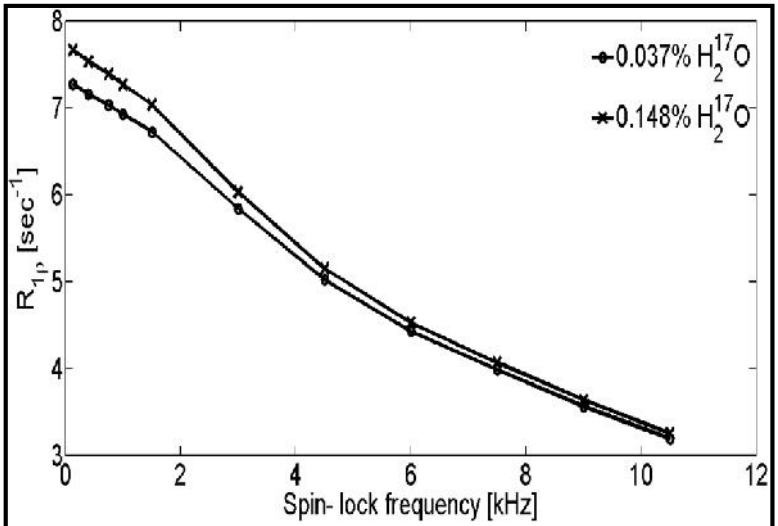


**Figure 6**: The dispersion curves for phantoms 1 (natural abundance $H_2{}^{17}O$) and 2 (four times natural abundance).

The $R_{1\rho}(\omega)$ can be related to $H_2{}^{17}O$ concentration using the following equation(13)

$$R_{1\rho}(\omega) = R^{\circ}{}_{1\rho}(\omega) + r_{1\rho}(\omega)(f_s) \qquad (7)$$

where $R^{\circ}{}_{1\rho}(\omega)$ is the inverse $T^{\circ}{}_{1\rho}(\omega)$ without $H_2{}^{17}O$ present in the sample, $f_s$ is the concentration of $H_2{}^{17}O$ in a given sample and $r_{1\rho}(\omega)$is the relaxivity of $H_2{}^{17}O$. If we consider the $R_{1\rho}(\omega)$ at natural abundance and some enriched fraction the difference between the $R_{1\rho}(\omega)$ rates can be expressed as:

$$R_{1\rho}(\omega)_E - R_{1\rho}(\omega)_{NA} = r_{1\rho}(\omega)((f_E) - (f_{na})) \quad (8)$$

where $(R_{1\rho})_{NA}$ is the $R_{1\rho}$ relaxation rate at natural abundance, $(R_{1\rho})_E$ is the relaxation rate due to the enhancement of $H_2{}^{17}O$, and $f_E$ and $f_{NA}$ are the enriched and natural abundance concentrations, respectively. Equation 8 can be used, with the experimentally determined values of $(R_{1\rho})_{NA}$, $(R_{1\rho})_E$, and the known values of $f_E$, and $f_{NA}$, to calculate the relaxivity values at each spin lock power.

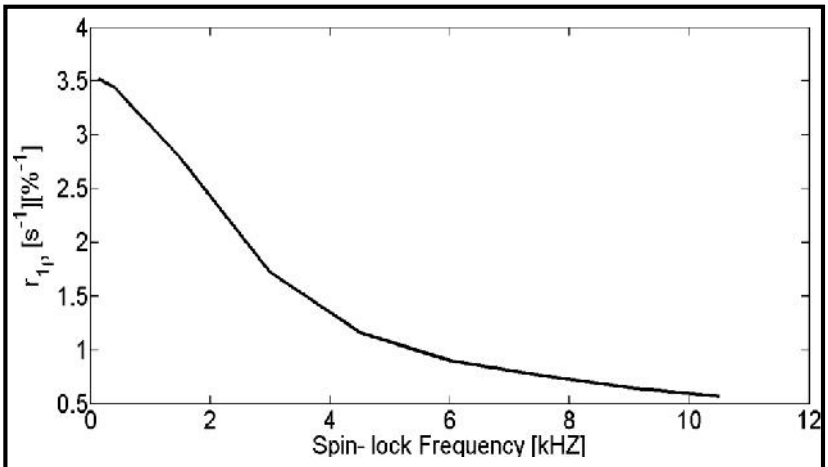


**Figure 7**:The relaxivity of $H_2{}^{17}O$ as function of spin lock frequency.

As shown in **Figure 7**, the relaxivity of $H_2{}^{17}O$ decreases with increasing spin locking frequency. The values for the relaxivity of $H_2{}^{17}O$ at 2T in 7% BSA phantoms have been previously reported by Reddy (13). The relaxivity ($3.5s^{-1}\ \%^{-1}$) at the lower extrema (128HZ) of the spin lock frequencies (**Figure 7**) are very similar to those measured by Reddy et al ($3.4s^{-1}\ \%^{-1}$). However, at high spin lock frequencies Reddy's relaxivity values clearly approach zero (13) whereas ours decay to about 0.5 $s^{-1}\ \%^{-1}$ at a spin lock frequency of 10,500Hz. This suggests that $H_2{}^{17}O$ relaxivity is greater at high (main) magnetic field strengths, such as that used herein. Consequently, this could reduce the reliability of quantifying the amount of $H_2{}^{17}O$ using Eq. 6, since the data retains some sensitivity to exchange at the high spin locking frequency.

An assumption frequently utilized with the two-frequency approach (as described by Eq.6) is that $T_{1\rho o}$ is very close to the natural abundance $T_{1\rho}$ ($T_{1\rho}$ NA) such that one can replace $T_{1\rho o}$ with $T_{1\rho}$ NA in equation 6 (13). Our data shows the values of these two parameters are very close as the maximum percent difference between these two values was 1.83% (**Table 2**). Thus, there was very little difference between $T_{1\rho o}$ and $T_{1\rho}$ NA over the entire frequency range. $T_{1\rho o}$ was determined by using the values of the relaxivity at each frequency calculated from equation 8 and then putting them into equation 7 to determine $T_{1\rho o}$.

**Table 2**: Intrinsic and Natural Abundance $T_{1\rho}$ values of 7% BSA phantoms at pH 7.4.

| Spin lock frequency | $R_{1\rho o}$ | $R_{1\rho}$ NA | % difference |
|---|---|---|---|
| 128HZ | 7.1431 | 7.274 | 1.83 |
| 400HZ | 7.0274 | 7.151 | 1.70 |
| 750HZ | 6.9161 | 7.033 | 1.69 |
| 1000HZ | 6.8064 | 6.924 | 1.72 |
| 1500HZ | 6.6194 | 6.724 | 1.58% |

| **Table 2**: cont. | | | |
|---|---|---|---|
| 3000HZ | 5.7772 | 5.839 | 0.98% |
| 4500HZ | 4.9785 | 5.018 | 0.78% |
| 6000HZ | 4.3958 | 4.426 | 0.69 |
| 7500HZ | 3.9531 | 3.983 | 0.76 |
| 9000HZ | 3.5374 | 3.565 | 0.78 |
| 10500HZ | 3.1697 | 3.193 | 0.72 |

To evaluate the enrichment fraction of each phantom using the two-frequency approach we first inserted the raw signal data (for signals acquired with 250 Hz and 10500Hz) into Eq. 6, as is the typical approach used by others, but this proved unreliable as the extracted values were erratic as shown in **Table 3**. A plausible explanation for this is that relaxivity does not decay to zero at high spin locking frequencies as is assumed with the two-frequency approach. As described above, our relaxivity data (at 9.4T) agrees very well with previous studies (at 2T) for low frequencies but does not decay as rapidly as the frequency is increased(13). This is further confounded by the observation that when the spin lock frequency is increased to beyond 20 kHz the relaxivity is essentially the same as that measured around 10kHz, indicating we have hit the noise floor for the relaxivity measurements. However, as shown in **Table 3**, we could extract reasonable enrichment fractions if we first fit the signals to Eq. 4 and used the fitted signal values

in Eq. 6. Given the quality and similarity of the fits to the raw signals it is still not completely clear why only the fitted data returned reasonable enrichment fractions.

To ensure that our high frequency data had minimal sensitivity to exchange we selected values where the second derivative of the $R_{1\rho}$ versus frequency curve were well beyond the inflection point (**Figure 8**), as this point is representative of the mean exchange rate.

**Table 3**: Calculation of fraction enhancement of $H_2{}^{17}O$ ($f_e/f_{na}$) in phantom pair at pH 7.4 (phantoms 1 and 2). The correct value of 4 was most accurately produced using the fitted signal decays from the data with spin lock time of 1s. The raw signal data yielded erratic results.

| Spin-Lock | $f_e/f_{na}$ (raw) SLT=0.25 | $f_e/f_{na}$(raw) SLT=1 | $f_e/f_{na}$ (fit) SLT=0.25 | $f_e/f_{na}$ (fit) SLT=1 |
|---|---|---|---|---|
| 6,000Hz | 1.0663 | 0.4916 | 2.7398 | 3.4424 |
| 7,500Hz | -0.4121 | 1.1083 | 2.9913 | 3.6312 |
| 9,000Hz | -0.3128 | 0.5107 | 3.3184 | 3.7597 |
| 10,500Hz | -0.25 | 0.5266 | 3.6214 | 3.8728 |

.

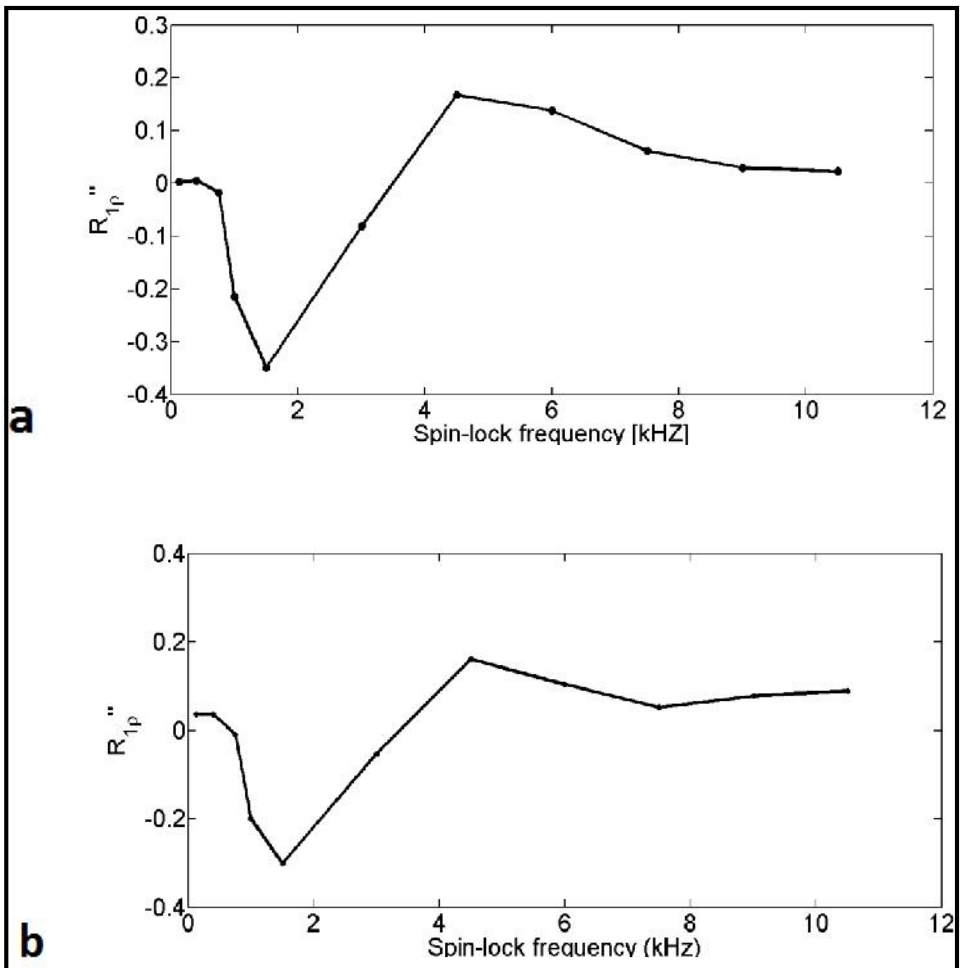


**Figure 8**: The second derivative of the $R_{1\rho}$ dispersion curve of phantom 1(a) and 8 (b). Points above 3 kHz are above the inflection point and accordingly these were used in the two frequency method.

For the two frequency approach, the fitted signal decays corresponding to the last spin lock time (1s) yielded the most accurate measurements of enrichment fraction (plotted in **Figure 9)**. This pattern was persistent throughout all of the phantoms (**Appendix A**). This is likely due to that fact the longer the spin-locking pulse is applied, the greater sensitivity magnetization has to exchange, as has been previously shown (12).

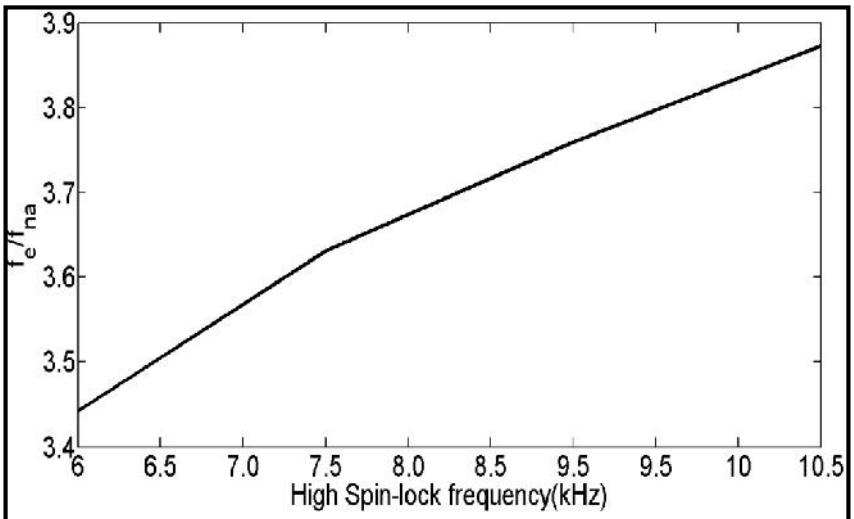


**Figure 9**: The fractional enrichment (with SLT=1) of between phantoms 1 and 2 as a function of high spin lock power.

We also examined the effect of pH on the $T_{1\rho}$ dispersion curves and quantification of enrichment fraction by changing the pH from 7.4 to 5.6 in two phantoms (phantoms 1 and 3, natural abundance [$H_2{}^{17}O$]) (**Figure 10**). The solution pH can substantially alter $T_{1\rho}$ dispersion by altering proton exchange between the water and protein pools. As a first step we evaluated phantoms with the same concentration (NA) of

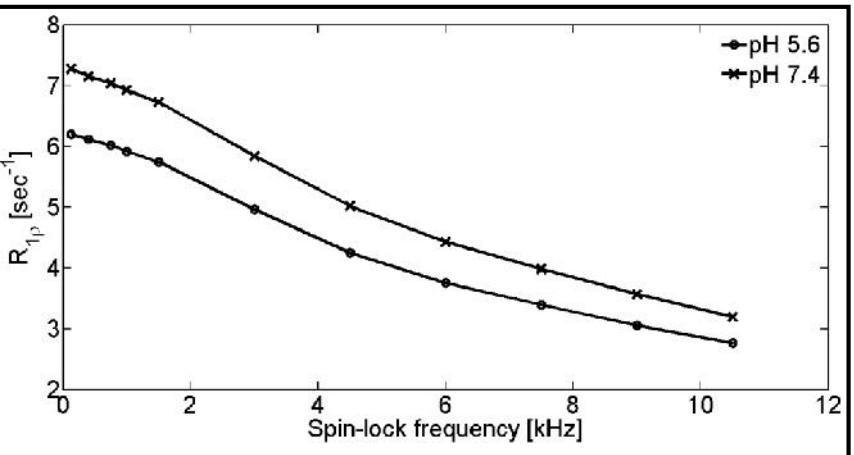


**Figure 10**: The effect of an acidic pH on $T_{1\rho}$ dispersion curves. The lower dispersion curve corresponds to a phantom with pH 5.6 and the higher curve to a phantom with pH 7.4.

$H_2{}^{17}O$ but different pH levels. As previously shown in BSA phantoms the exchange regimes between water and liable BSA protons are as follows: slow regime (pH ≤5.9), intermediate (pH 6.4-7.9), fast (pH≥8.4) (15). Studies have shown that $T_{1\rho}$ is most sensitive to proton exchanges in the intermediate regime (12, 15). We found that as pH is changed from 7.4 to 5.6, the $R_{1\rho}$ values decreased (**Figure 10**). Consequently, our results are consistent with previous studies (15) as this change shows that the sensitivity $R_{1\rho}$ to exchange decreased going from a pH in the intermediate (7.4) to the slow (5.6)regime.

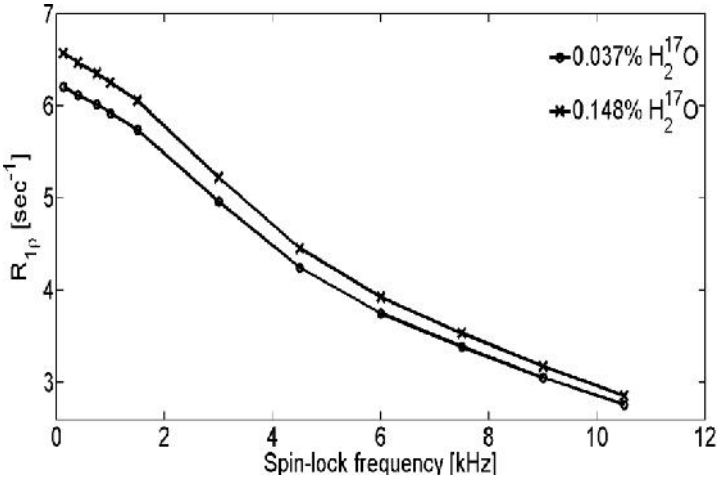


**Figure 11**: The effect of $H_2{}^{17}O$ enrichment on a BSA phantom at pH 5.6.

We next investigated the influence of varying pH on the computation of $H_2{}^{17}O$ enrichment using a similar pair of phantoms with pH 5.6 (**Figure 11**). The magnitude of the shift due to $H_2{}^{17}O$ contrast was similar to that in the phantoms at the physiological pH. Likewise, the pH change had only a slight impact on quantification of $H_2{}^{17}O$ enrichment. For the two frequency method, with a high spin lock power of 10,500Hz the enrichment fraction was computed to be 3.62, yielding an error of 9.5% as compared to 3.25% for the phantoms at physiological pH. The ratio of $f_e/f_{na}$ at each of the 11 spin lock

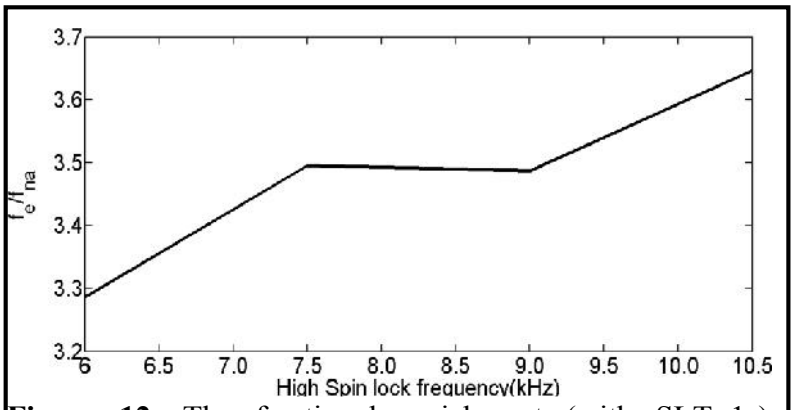


**Figure 12**: The fractional enrichment (with SLT=1s) between phantoms 3 and 4 .

frequencies is shown in **Figure 12**.

We next examined the effect of changing $T_1$ and $T_2$ on the $T_{1\rho}$ dispersion and quantification of enrichment fraction. As aforementioned, $T_{1\rho}$ values approach $T_2$ as the spin lock power approaches 0 and $T_1$ as the spin lock power approaches the lamor frequency. Consequently, altering the $T_1$ and $T_2$ times of the phantoms will change the $T_{1\rho}$ values. For our phantoms, we changed the $T_1$ and $T_2$ values by adding Gadopentetic acid (Gd-DTPA). Gd-DTPA is a paramagnetic contrast agent which is known to change $T_1$ and $T_2$ according to the following relations (16):

$$\frac{1}{T_1} = \frac{1}{T_1^{\circ}} + r_1[\text{GdDTPA}] \quad (9)$$

$$\frac{1}{T_2} = \frac{1}{T_2^{\circ}} + r_2[\text{GdDTPA}] \quad (10)$$

The literature reported values of the relaxivity of Gd-DTPA are $r_1$=3.79 $mM^{-1}s^{-1}$ and $r_2$=13.9$mM^1s^{-1}$(16). Here, $T_1^{\circ}$ and $T_2^{\circ}$ represent the relaxation rates for a 7% BSA solution without Gd-DTPA in it.1 /$T_1^{\circ}$ and 1/$T_2^{\circ}$ were estimated to be 0.39 $s^{-1}$ and 8$s^{-1}$,respectively (17). Thus, with the addition of 0.25mM of Gd-DTPA the 1/$T_1$ and 1/$T_2$ should increase to 1.382$s^{-1}$ and 11.4750$s^{-1}$, respectively. The effect of the Gd-DTPA (at pH 7.4) on $T_{1\rho}$ dispersion was quite different than that of $H_2{}^{17}O$

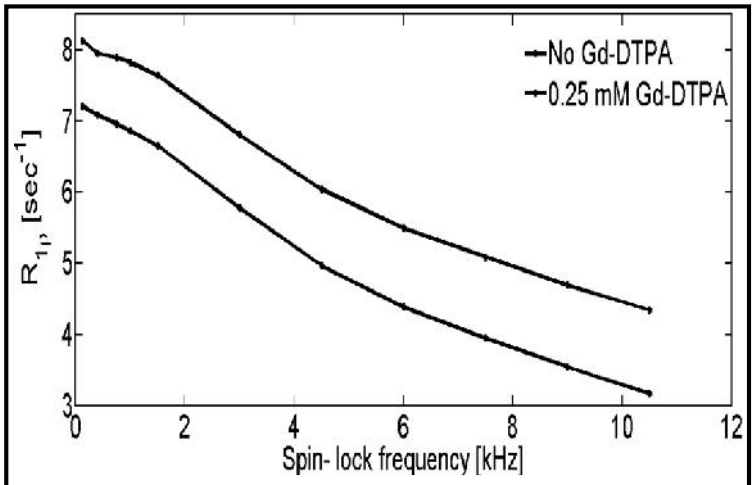


**Figure 13:** Effect of Gd-DTPA enhancement of the $T_{1\rho}$ dispersion. The lower graph is phantom 1 and the upper graph is phantom 5.

enrichment (**Figure 13**).With Gd-DTPA, the magnitude of the shift in the $R_{1\rho}$ values was the nearly same at low and high frequencies., owing to the influence of Gd-DTPA on both $T_1$ and $T_2$ values whereas $H_2{}^{17}O$ primarily alters the relaxation at low spin locking frequencies.

To examine the effect of Gd-DTPA on the quantification of $H_2{}^{17}O$ enrichment at pH 7.4 we created an enriched and unenriched phantoms with a Gd-DTPA concentration of 0.25mM. Similar to the phantoms without Gd-DTPA, the amount of change seen in the dispersion due to $H_2{}^{17}O$ enrichment was greatest at low frequencies and lowest at high frequencies (**Figure 14**). Unlike the pH study, the quantification of $H_2{}^{17}O$ was greatly impacted by the Gd-DTPA addition as shown in **Figure 15**. At 10,500Hz, the value of $f_e/f_{na}$is 2.3 which gives an error of 42%.

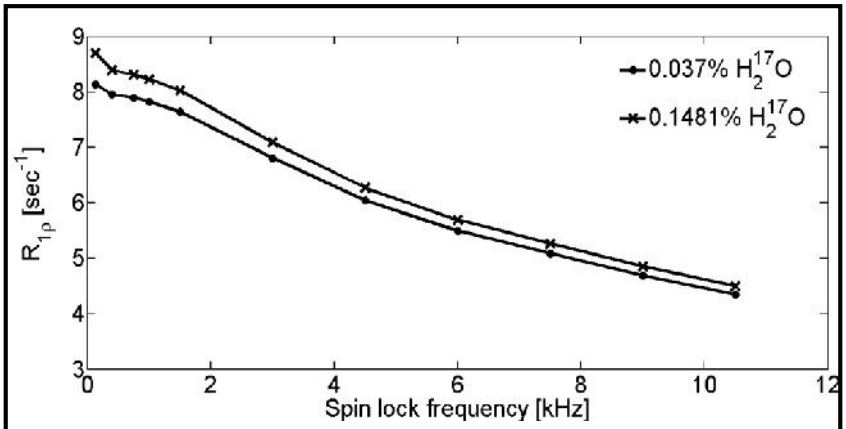


**Figure 14**: The effect of $H_2{}^{17}O$ enrichment on a BSA phantom enriched with Gd-DTPA at 0.25mM.

We also examined the simultaneous impact of Gd-DTPA enhancement (at 0.25mM) and acidic pH

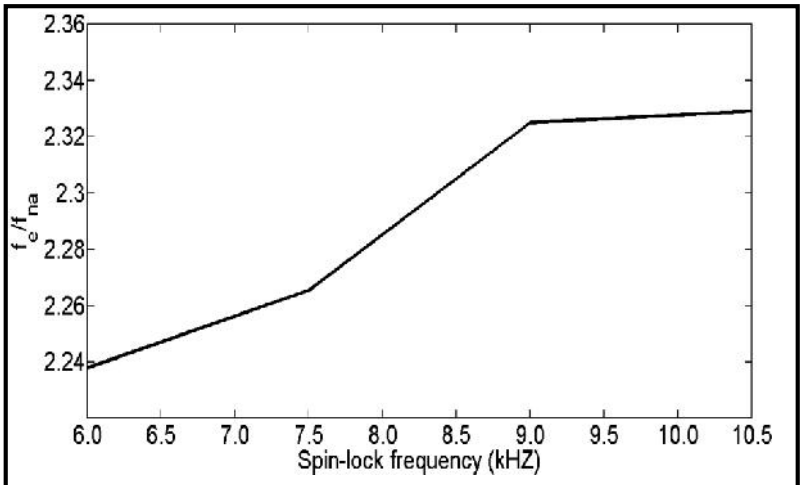


**Figure 15**: The fractional enrichment (with SLT=1s) between phantoms 5 and 6 as a function of high spin lock power

(5.6) on ratio $f_e/f_{na}$ between an enriched and unenriched phantom pair (**Figure 17**). Again, equation 6 proved highly inaccurate with the 10,500Hz high spin lock power yielding a value of 2.6 for $f_e/f_{na}$ or 35% error.

The high quality of the curve fits (**Appendix B**) as well as the high repeatability of these measurements gives us confidence in the $T_{1\rho}$ values. Additionally, the dispersion curve for phantom 1 nearly matches a dispersion reported for an almost identical phantom (8% BSA, pH 7.4) reported by Makela et. al(17). Unfortunately, there is paucity of studies of on BSA at high (main) field and to our knowledge, no studies on the quantification of $H_2{}^{17}O$ at 9.4T. As such, it is difficult for us to have a basis to access the validity of the $H_2{}^{17}O$ quantification. Consequently, further studies will be needed to

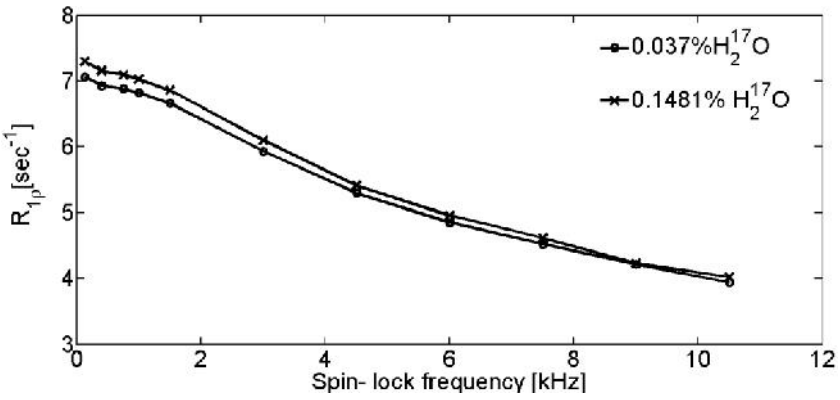


**Figure 16**: Effect of Gd-DTPA and pH enhancement. The lower graph is phantom 7 and the upper graph is phantom 8.

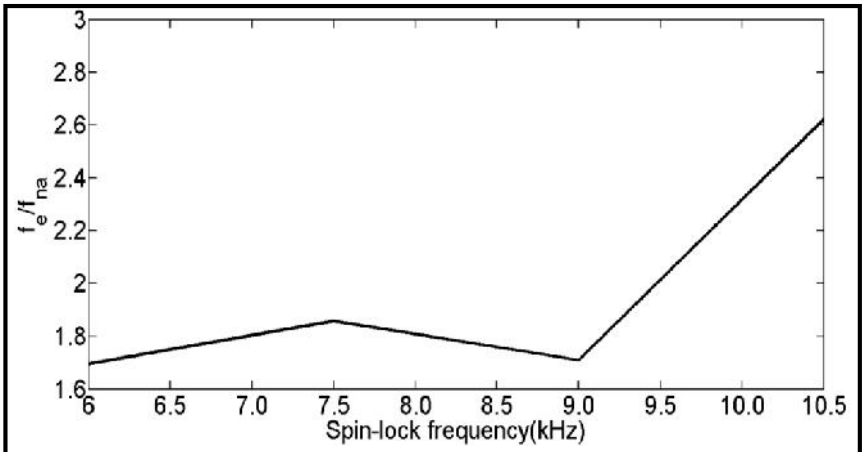


**Figure 17**: The fractional enrichment (with SLT=1s) between phantoms 7 and 8 as a function of high spin lock power.

determine if the reported problems (particularly in the context of variable $T_1$ and $T_2$) of this technique hold at low (clinical) field strengths.

**2.4 Discussion**

This study examined the influence of an acidic conditions and heterogeneous $T_1$ and $T_2$ profiles on the quantification of $H_2{}^{17}O$. The quantification of $H_2{}^{17}O$ was relatively insensitive to pH but very sensitive to changes in $T_1$ and $T_2$ profiles. The insensitivity of the two- frequency method to pH has a possible explanation in the context of previous work by Meiboom (18). In these studies, the difference $(1/T_2\text{-}1/T_1)$ of water protons (exchanging between $H_2{}^{17}O$ and $H_2{}^{16}O$) as a function of pH was determined through experiments (**Figure 18**). It should be noted that $T_{1\rho}$ dispersion curves are the sum of all proton exchange processes that are occurring. However, it is the exchange between $H_2{}^{17}O$ and $H_2{}^{16}O$ to which equation 6 is sensitive. The plot corresponding to this experiment shows that the value of $1/T_2\text{-}1/T_1$ at pH 5.6 is nearly identical to that at 7.4 (**Figure 18**). The implication of this is that the contribution of the exchange between $H_2{}^{17}O$ and $H_2{}^{16}O$ to$1/T_2\text{-}1/T_1$, and consequently, $T_{1\rho}$ dispersion, is unaffected by the pH change. We have also learned that the two frequency method is highly sensitive to changes in the $T_1$ and $T_2$ profiles of the phantoms. Adding Gd-DTPA lead to marked errors in the computation of the enrichment fraction of $H_2{}^{17}O$ water in both phantoms pairs. An explanation for this is that since both $T_1$ and

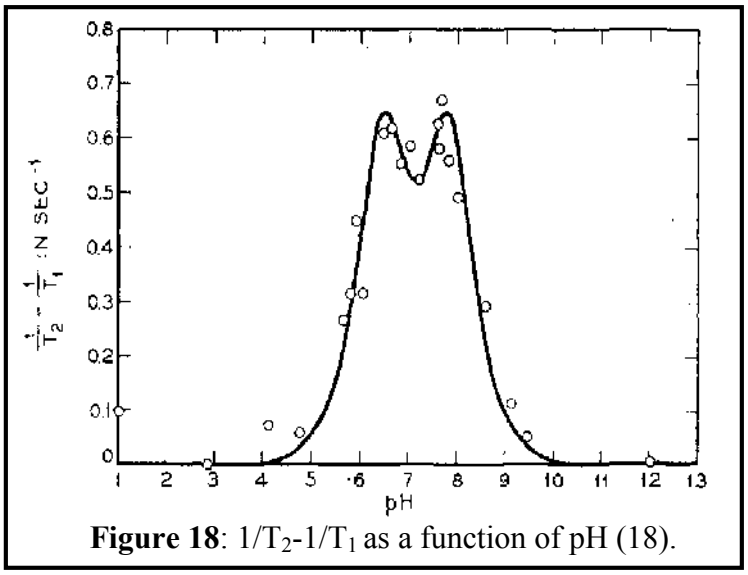

**Figure 18**: $1/T_2\text{-}1/T_1$ as a function of pH (18).

$T_2$ are changing (in a non linear way) the difference ($1/T^{l}_{1\rho o} - 1/T^{h}_{1\rho o}$) in equation 6 changes such the it renderers the quantification inaccurate.

# CHAPTER 3

# SYNOPSIS AND CONCLUSIONS

## 3.1 Reliability of $T_{1\rho}$ based measures of Oxygen Metabolism

Our data has important implications for assessing $H_2{}^{17}O$ content using the two frequency $T_{1\rho}$ approach. We found that at high field strengths the relaxivity decays much more slowly as compared to the lower field strengths currently used in practice. As a consequence of this, the high spin lock power must be acquired at a very high power to fully decouple the exchange mechanism of $H_2{}^{17}O$ with $H_2{}^{16}O$ from the $T_{1\rho}$ relaxation of water protons. Even after acquiring data at very high power (e.g 20,000Hz) the relaxivity at 9.4T(0.1 $s^{-1}\%^{-1}$) still did not reach the lower limits of that observed at 2T(<<1). The latter could limit successful use of equation 6 because the upper limit of stable CW RF power on most animal MRI scanners is around 20,000Hz (19). As a consequence of this, it could be difficult to use such scanners to achieve the high spin lock powers that appear necessary to quantify $H_2{}^{17}O$ at this field strength. Furthermore, our in vitro measurements were successful only after we used the fitted values of the signal decay as opposed to raw data; also after we used the actual values of $1/T_{1\rho o}$ instead of the approximating the value of $1/T_{1\rho o}$ by $1/T_{1\rho}$ (NA). Since it is impossible to determine $1/T_{1\rho o}$ *in vivo* and difficult to compare our results with the literature by using the fits, a future step would be to make these measurements at lower field strengths in order to reevaluate these issues. It is important to note that the resolution of these issues is important if we aim to accurately measure $[H_2{}^{17}O]$ and tumor oxygen utilization.

### 3.2Future direction of Research

We have examined the reliability of the two-frequency $T_{1\rho}$ approach for quantifying [$H_2{}^{17}O$] *in vitro*. It would be useful to consider more phantoms that better approximate the tumor microenviorment. One way to do this is to create phantoms of varying protein composition. Cancer cells are known to have a heterogeneous and dynamic protein composition. An example of this type of experiment would be to see how making a phantom consisting of 3.5% BSA and 3.5% glutamine. Such protein heterogeneity could influence exchange within the water pool which in turn could impact in vivo quantification. It would also be relevant to look at crosslinking. In all of our phantoms the inflection point did not change which shows that the mean exchange did not change. However, to better mimic the tumor microenviorment one should take inflection shifts into account. Varying the amount of crosslinking (changing the concentration of gluteraldehyde) would be a good way to examine how inflection shifts influence quantification of $H_2{}^{17}O$ because crosslinking is known to change inflection (20).

This work suggests that changing pH does not affect the reliability of measurements of $H_2{}^{17}O$ but changing $T_1$ and $T_2$ does. Given the heterogeneous nature of tumor microenviorment the physiological changes that occur in cancerous tissue could possibly affect $T_1$ and $T_2$. It is thus imperative to further investigate phantoms in which $T_1$ and $T_2$ are altered by methods other Gd-DTPA addition. This knowledge will yield great insight into the scope of which changes in $T_1$ and $T_2$ affects $H_2{}^{17}O$ quantification in the context of understating the rate oxygen metabolism in cancer as well as other diseases where oxygen metabolism is implicated.

## APPENDIX A

Phantom pair pH 7.4

| SLA | $R_{1\rho o}$ | $f_e/f_{na}$(fit,SLT=0.25s) | $f_e/f_{na}$(fit,SLT=1s) | $f_e/f_{na}$ (raw,SLT=0.25s) | $f_e/f_{na}$ (raw,SLT=0.25s) |
|---|---|---|---|---|---|
| 6,000HZ | 4.3958 | 2.7398 | 3.4424 | 1.0663 | 0.4916 |
| 7,500HZ | 3.9631 | 2.9913 | 3.6312 | -0.4121 | 1.1083 |
| 9,000HZ | 3.5374 | 3.3184 | 3.7597 | -0.3128 | 0.5107 |
| 10,500HZ | 3.1697 | 3.6214 | 3.8728 | -0.25 | 0.5266 |

Phantom pair 5.6

| SLA | $R_{1\rho o}$ | $f_e/f_{na}$(fit,SLT=0.25s) | $f_e/f_{na}$(fit,SLT=1s) | $f_e/f_{na}$ (raw,SLT=0.25s) | $f_e/f_{na}$ (raw,SLT=0.25s) |
|---|---|---|---|---|---|
| 6,000HZ | 3.6962 | 2.387 | 3.286 | -1.223 | 0.4417 |
| 7,500HZ | 3.3388 | 2.6116 | 3.4953 | -1.0619 | 0.4343 |
| 9,000HZ | 3.0176 | 2.7505 | 3.4871 | -0.9813 | 0.4243 |
| 10,500HZ | 2.727 | 3.0207 | 3.6464 | -0.9874 | -0.4197 |

Phantom pair 7.4, 0.25 Gd-DTPA

| SLA | $R_{1\rho o}$ | $f_e/f_{na}$(fit,SLT=0.25s) | $f_e/f_{na}$(fit,SLT=1s) | $f_e/f_{na}$ (raw,SLT=0.25s) | $f_e/f_{na}$ (raw,SLT=1s) |
|---|---|---|---|---|---|
| 6,000HZ | 5.4229 | 2.0774 | 2.238 | 19.9132 | 1.0449 |
| 7,500HZ | 5.0209 | 2.1167 | 2.2655 | 85.202 | 1.0207 |
| 9,000HZ | 4.6329 | 2.2062 | 2.3251 | -24.0041 | 0.9961 |
| 10,500HZ | 4.2948 | 2.2338 | 2.32911 | -14.1399 | 0.998 |

Phantom pair 5.6, 0.25 Gd-DTPA

| SLA | $R_{1\rho o}$ | $f_e/f_{na}$(fit,SLT=0.25s) | $f_e/f_{na}$(fit,SLT=1s) | $f_e/f_{na}$ (raw,SLT=0.25s) | $f_e/f_{na}$ (raw,SLT=1s) |
|---|---|---|---|---|---|
| 6,000HZ | 4.8105 | 1.5736 | 1.6956 | -1.0296 | -8.7077 |
| 7,500HZ | 4.4848 | 1.6453 | 1.8578 | 4.9719 | -8.2761 |
| 9,000HZ | 4.2063 | 1.6256 | 1.71 | 7.326 | -5.7071 |
| 10,500HZ | 3.914 | 1.7057 | 2.6216 | 16.7803 | -4.1094 |

## APPENDIX B

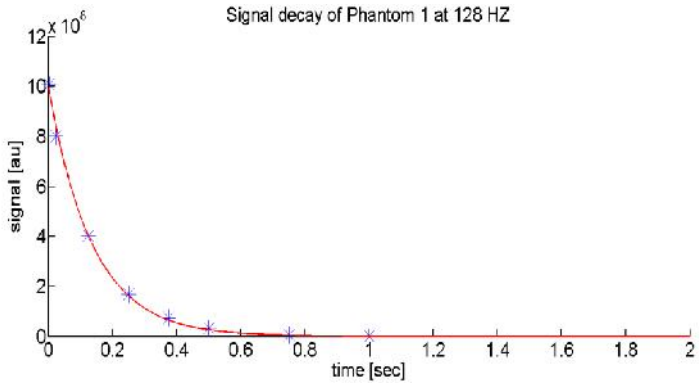
Signal decay of Phantom 1 at 128 HZ
x 10^6
signal [au]
time [sec]

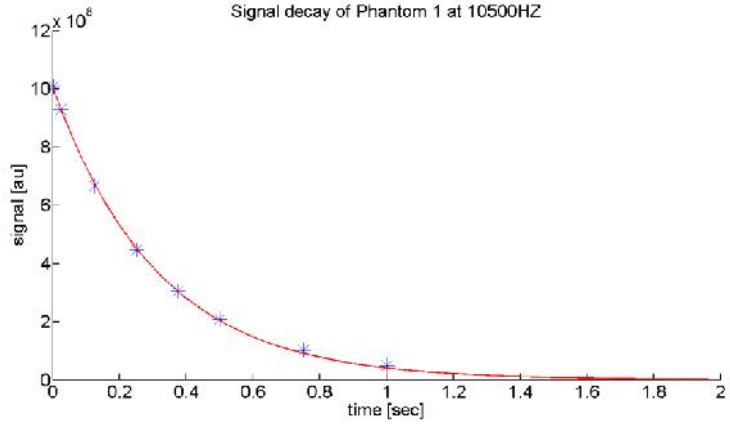
Signal decay of Phantom 1 at 10500HZ
x 10^8
signal [au]
time [sec]

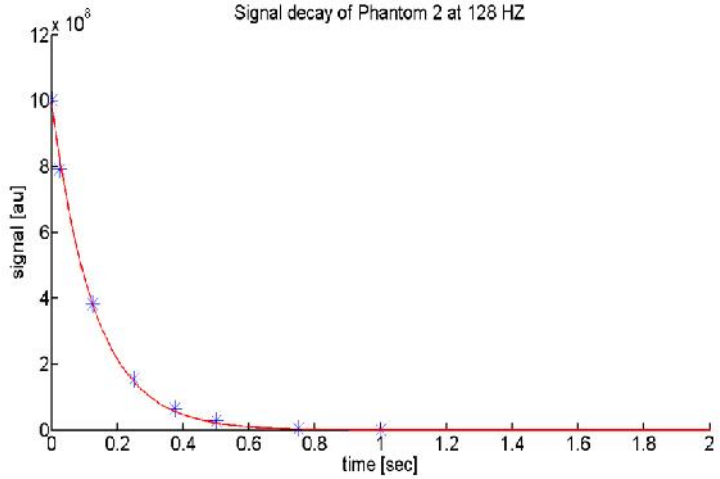
Signal decay of Phantom 2 at 128 HZ
x 10^8
signal [au]
time [sec]

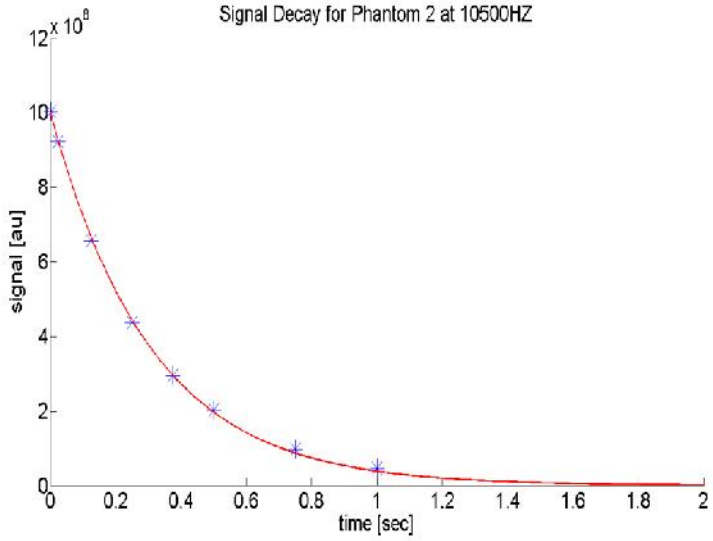
Signal Decay for Phantom 2 at 10500HZ
x 10^8
signal [au]
time [sec]

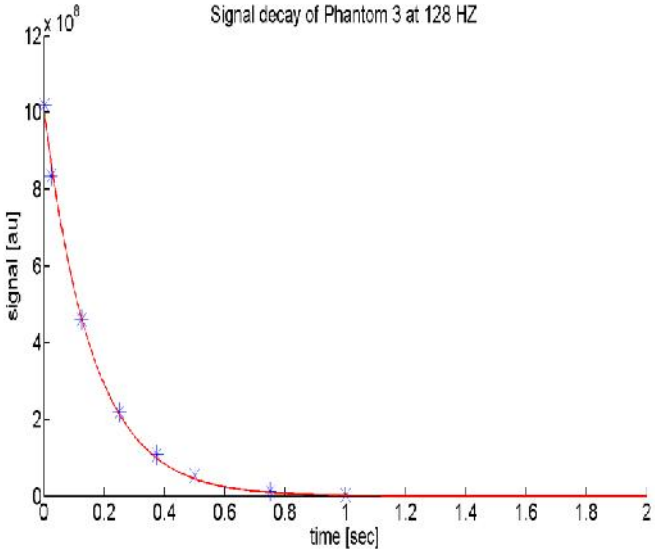
Signal decay of Phantom 3 at 128 HZ
x 10^8
signal [au]
time [sec]

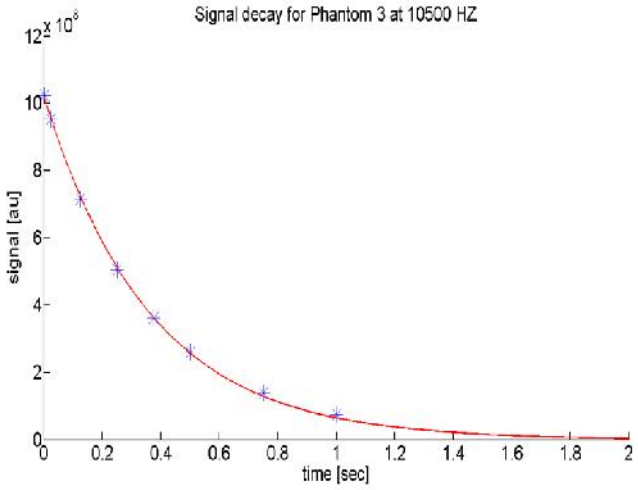
Signal decay for Phantom 3 at 10500 HZ
x 10^8
signal [au]
time [sec]

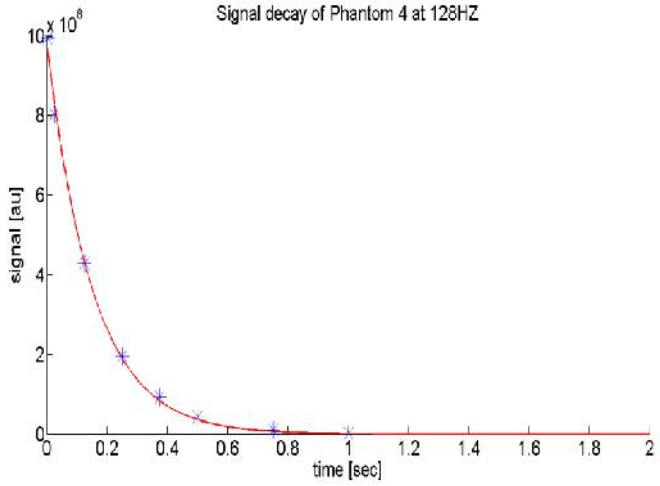
Signal decay of Phantom 4 at 126HZ
x 10^8
signal [au]
time [sec]

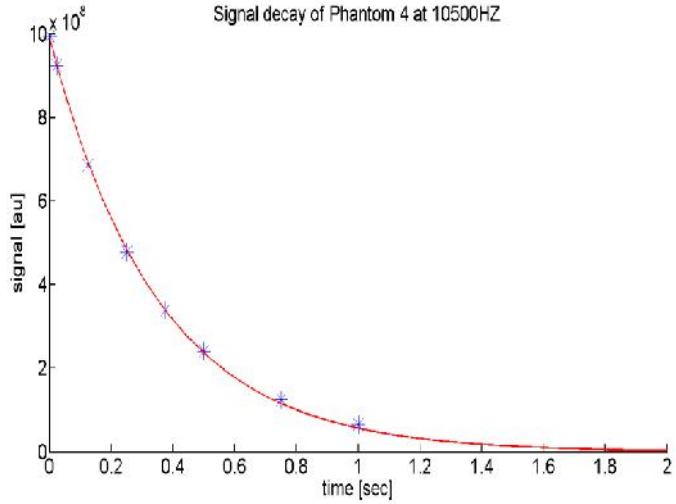
Signal decay of Phantom 4 at 10500HZ
x 10^8
signal [au]
time [sec]

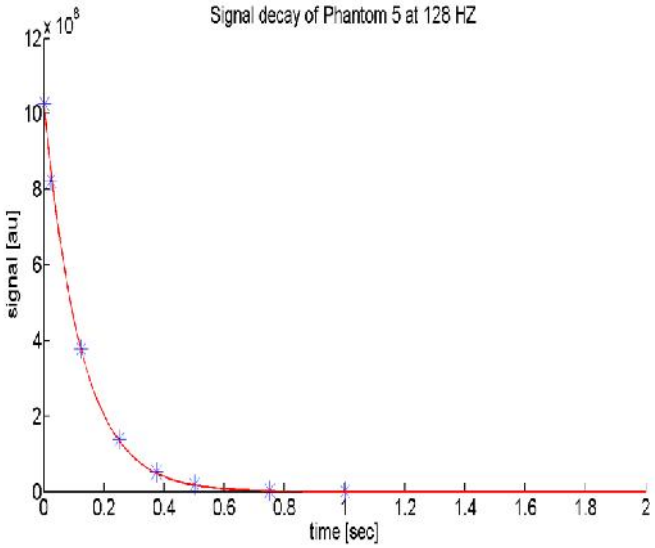
Signal decay of Phantom 5 at 128 HZ
x 10^8
signal [au]
time [sec]

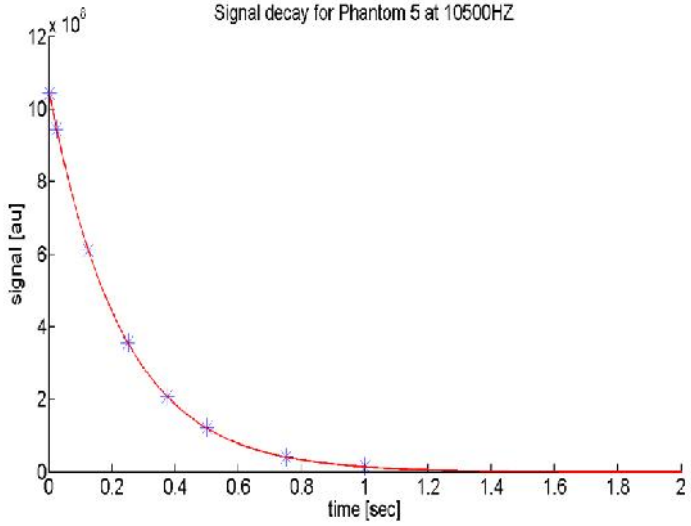
Signal decay for Phantom 5 at 10500HZ
x 10^6
signal [au]
time [sec]

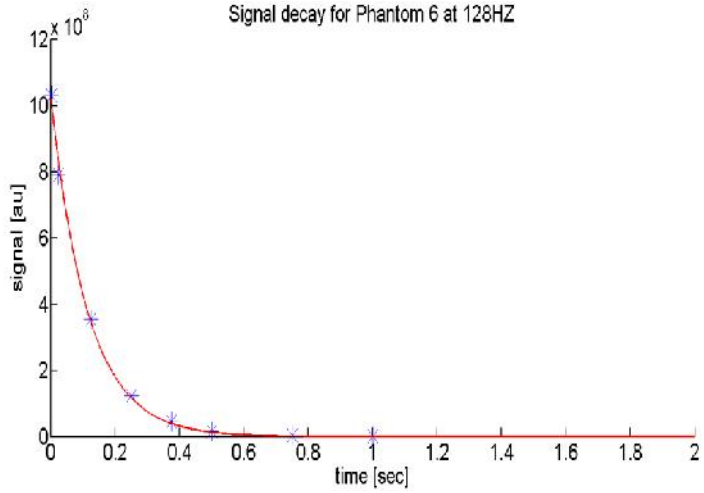
Signal decay for Phantom 6 at 128HZ
x 10^6
signal [au]
time [sec]

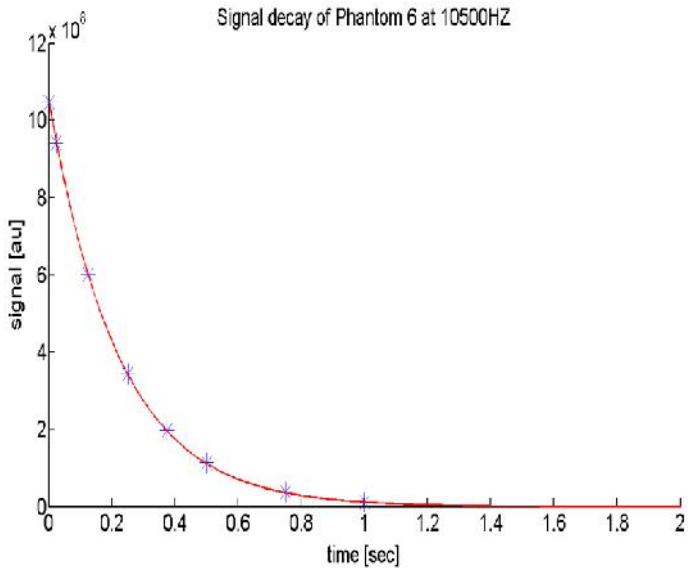
Signal decay of Phantom 6 at 10500HZ
x 10^6
signal [au]
time [sec]
0
2
4
6
8
10
12
0.2
0.4
0.6
0.8
1
1.2
1.4
1.6
1.8
2

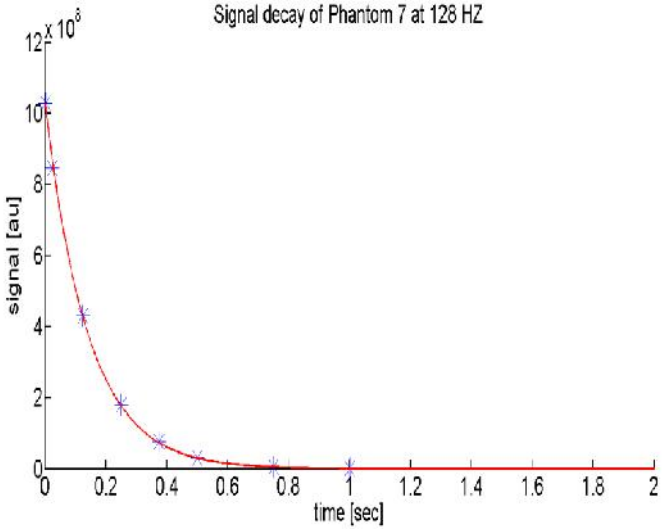
Signal decay of Phantom 7 at 128 HZ
x 10^6
signal [au]
time [sec]
0
2
4
6
8
10
12
0.2
0.4
0.6
0.8
1
1.2
1.4
1.6
1.8
2

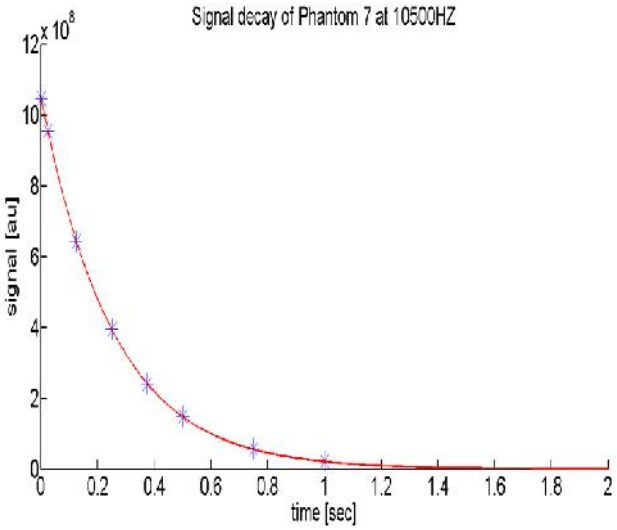
Signal decay of Phantom 7 at 10500HZ
x 10^8
12
10
8
6
4
2
0
signal [au]
0
0.2
0.4
0.6
0.8
1
1.2
1.4
1.6
1.8
2
time [sec]

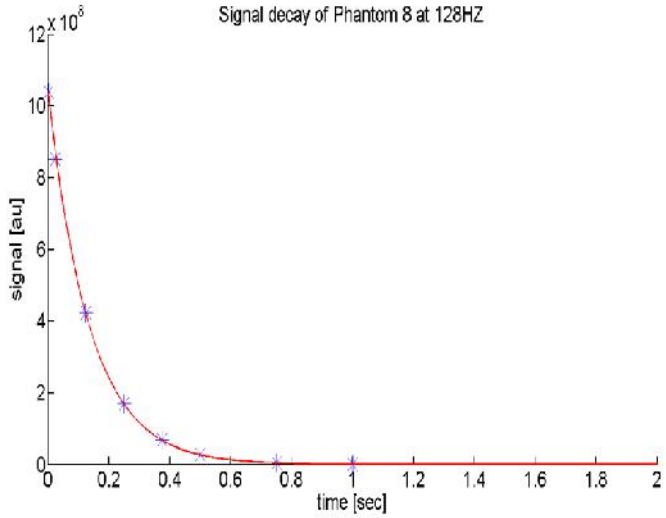
Signal decay of Phantom 8 at 128HZ
x 10^8
12
10
8
6
4
2
0
signal [au]
0
0.2
0.4
0.6
0.8
1
1.2
1.4
1.6
1.8
2
time [sec]

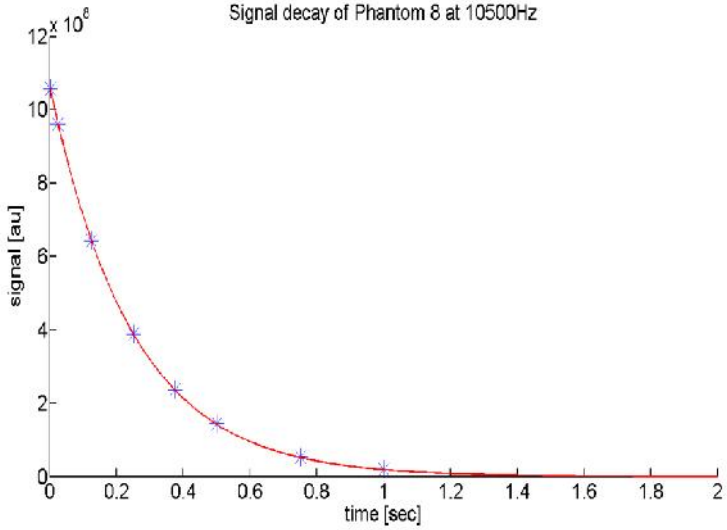
Signal decay of Phantom 8 at 10500Hz
x 10^8
12
10
8
6
4
2
0
signal [au]
0
0.2
0.4
0.6
0.8
1
1.2
1.4
1.6
1.8
2
time [sec]

## REFERENCES


[1] Vander Heiden, M., Cantley, L., Thompson, C., ( 2009) *Understanding the Warburg Effect:The Metabolic Requirements of Cell Proliferation.* Science **324,** 1029 (2009)

[2]Dang, C., Semenza, G *Oncogentic alterations of metabolism* Trends Biochem Sci **24,** 68(1999)

[3] Kavanagh, M.C., Tsang,V.,Chow, S.et al *A comparison in individual murine tumors of techniques for measuring oxygen levels.* Int. J. Radiology Biol. Phys. **44,** 1137(1999)

[4]Hustinx, R., Eck, S.L., Alavi, Abass *Potential Applications of PET Imaging in Developing Novel Cancer Therapies*, The Journal of Nuclear Medicine*,***40**, 996(1996)

[5] Zhu, X., Zhang, Y., Tian, R., Lei, H, Zhang, N, Zhang, X Merkle, H Ugurbil K, Chen W., (2002) *Development of (17)O NMR approach for fast imaging of cerebral metabolic rate of oxygen in rat brain at high field*, Proc Natl Acad Sci USA **99,** 13194 (2002)

[6] Zhu, X., Zhang, Y., Tian, R., Lei, H, Zhang, N, Zhang, X Ugurbil K, Chen W., In vivo $^{17}O$ *NMR approaches for brain study at high field*, NMR in Biomedicine*,* **18,** 103(2005)

[7] Rule,G.S., Hitchens,T.K, *Fundamentals of Protein NMR Spectroscopy,* Spinger, Dordrecht, Netherlands

[8] Ronen I, Merkle H, Ugurbil K, Navon G (1995*) Imaging of H217O distribution in the brain of a live rat by using proton-detected 17O MRI*, Proc. Natl Acad. Sci. USA, **95,** (1995) 12934

[9] Ravinder Reddy $T_{1\rho}$ Imaging: Techniques and Basis for Image Contrast

[10]Charagundla, S. $T_{1\rho}$–weighted magnetic resonance imaging: Principles and Diagnostic Application, 32(2004)

[11]Tailor, D.R., Poptani,H., Glickson, J.D., Leigh,J.S.,Reddy,R., *High-Resolution Assessment of Blood Flow in Murine RIF-1Tumors by Monitoring Uptake of $H_2{}^{17}O$ with Proton Weighted Imaging*. Magnetic Resonance in Medicine*,***49,** 1**(**2003)

[12]Kogan,F., Singh,A., Cai,K.,Haris,M.,Hariharon,H.,Reddy,R., *Investigation of Chemical exchange rate Using a combination of Chemical Exchange Saturation Transfer (CEST) and Spin-Locking Methods (CESTrho).* Magnetic Resonance in Medicine*,* 1(2011)

[13] Reddy, R., Stolpen, A.H., Leigh (1995) Dectection of $^{17}O$ by Proton $T_{1\rho}$ Dispersion Imaging, Journal of Magnetic Resonance **108,** 276(1995)

[14] McComis K.S., He,X.,Abendschein,S.,Gupte,P.,Gropler, R.J., Zheng,J *Cardiac $^{17}O$ MRI:Toward Direct Quantification of Myocardial Oxygen Consumption* Magnetic Resonance in Medicine, **63,** 1442(2010)

[15]Jin,T., Autio, J.,Obata,T.,and Kim,S., *Spin-Locking Versus Chemical Exchange Saturation Transfer MRI for Investigating Chemical Exchange Process Between Water and Liable Metabolite Protons*. Magnetic Resonance in Medicine ,**65,**1448(2011)

[16]Caravan, P., Farrar, C.T., Frullano,L.,Uppal,R *Influence of Molecular parameters and inceasing magnetic field strength on relaxivity of gadolimium- and manganese based constrast agents* Contrast Media&Molecular Imaging, **4,** 89(2009)

[17]Makela,H., Vita,E., Grohn,Olli, H.J., Kettunen,M., *$B_0$ Dependence of On-resonance Longitudnal Relaxation time in the Rotating Frame ($T_{1\rho}$) in Protein Phantoms and Rat Brain in vivo*. Magenetic Resonance in Medicine,**51,**4(2004)

[18]Meiboom, S. *Nuclear Magnetic Resonance study of Proton Transfer in Water*, The Journal of Magnetic Resonance, **11,** 375**(**1961)

[19] Cobb,J., Xie,J.,Gore,J.C., *Contibutions of Chemical Exchange to $T_{1\rho}$ Dispersion in a Tissue Model* Magnetic Resonance in Medicine (2011)

[20]Chen, E.,Kim, R.J,*Magnetic Resonance Water Proton Relaxation in Protein Soutions and Tissue*:*$T_{1\rho}$ Dispersion Characterization*. **5,** 12(2010)